ACS OMEGA

Open Access

http://pubs.acs.org/journal/acsodf

Article

Single Crystalline α-Fe_2O_3 Nanosheets with Improved PEC Performance for Water Splitting

Parveen Garg, Lokanath Mohapatra, Ajay Kumar Poonia, Ajay Kumar Kushwaha, Kumaran Nair Valsala Devi Adarsh, and Uday Deshpande*

Cite This: *ACS Omega* 2023, 8, 38607−38618

Read Online

ACCESS | Metrics & More | Article Recommendations | Supporting Information

ABSTRACT: We report the photoelectrochemical (PEC) performance of a densely grown single crystalline hematite (α-Fe_2O_3) nanosheet photoanode for water splitting. Unlike expensive ITO/FTO substrates, the sheets were grown on a piece of pure Fe through controlled thermal oxidation, which is a facile low cost and one-step synthesis route. The sheets grow with a widest surface parallel to basal plane (0001). Iron oxide formed on Fe consisting of layer structure α-Fe_2O_3−Fe_3O_4−Fe is elucidated from GIXRD and correlated to spectral features observed in Raman and UV−vis spectroscopy. The top α-Fe_2O_3 nanosheet layer serves as a photoanode, whereas the conducting Fe_3O_4 layer serves to transport photogenerated electrons to the counter electrode through its back contact. Time-resolved photoluminescence (TRPL) measurements revealed significantly prolonged carrier lifetime compared to that of bulk. Compared to the thin film of α-Fe_2O_3 grown on the FTO substrate, ∼3 times higher photocurrent density (0.33 mA cm^{-2} at 1.23 V_{RHE}) was achieved in the nanosheet sample under solar simulated AM 1.5 G illumination. The sample shows a bandgap of 2.1 eV and n-type conductivity with carrier density 9.59 × 10^{17} cm^{-3}. Electrochemical impedance spectroscopy (EIS) measurements reveal enhanced charge transport properties. The results suggest that nanosheets synthesized by the simple method yield far better PEC performance than the thin film on the FTO substrate. The anodic shifts of flat band potential, delayed electron−hole recombination, and growth direction parallel to the highly conducting basal plane (0001) being some of the contributing factors to the higher photocurrent observed in the NS photoanode are discussed. Characterizations carried out before and after the PEC reaction show excellent stability of the nanosheets in an alkaline electrochemical environment.

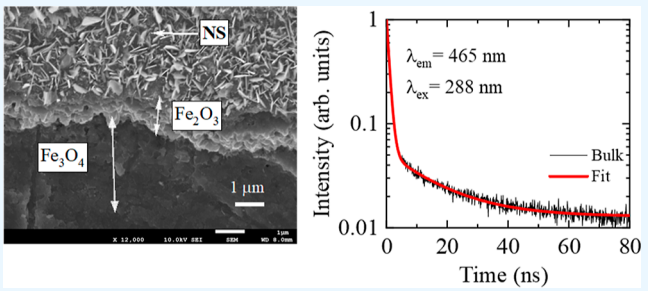

1. INTRODUCTION

Generation of hydrogen energy by means of water splitting through photoelectrochemical (PEC) reaction is sustainable and environmentally benign.[1] Splitting of water in a PEC cell was first reported in 1972 by Honda and Fujishima using TiO_2 as the photoanode under UV light.[2] An escalating research followed the finding, and the chemical vapor-deposited iron oxide film as a photoanode material for electrolysis of water was first investigated in 1976.[3] Since then, significant efforts have been made toward fabricating materials with good stability and PEC performance. Besides water splitting, hematite is also used for several other applications such as catalysis,[4,5] energy storage,[6] dye degradation,[7] oxygen reduction reaction,[4] gas sensing,[8,9] and so on. Hematite (α-Fe_2O_3) is widely studied as a photoanode for water oxidation owing to its low cost, nontoxicity, stability against photocorrosion and chemical corrosion, suitable band gap of 2.1 eV for visible light absorption, and positive valence band edge position vis-a-vis water oxidation potential.[10] The predicted efficiency of nearly 17% of hematite has been attracting researchers for decades.[11] This is more than the benchmark solar to hydrogen (STH) conversion efficiency of 10% required for practical applications.[12] However, maximum efficiency achieved could not meet the benchmark STH efficiency.[13] The PEC activity of the hematite photoanode is limited by several factors such as poor electrical conductivity (∼10^{-14} Ω^{-1} cm^{-1}),[14] short excited state carrier lifetime (∼10^{-12} s),[15] short hole diffusion length (2−4 nm),[16] and poor minority charge carrier (hole) mobility (0.031 cm^2 V^{-1} s^{-1}).[17]

Numerous strategies were employed to improve experimental STH efficiency of the α-Fe_2O_3 photoanode, such as nanostructuring, doping,[10] surface passivation layer,[18] cocatalyst,[19] composites,[20] and heterostructure.[21] These include high aspect ratio nanostructures,[22] which improves charge separation and suppresses electron−hole recombination.[23] Efficient

Received: August 4, 2023
Accepted: September 22, 2023
Published: October 8, 2023

electron transport is observed in α-Fe_2O_3 nanotubes, owing to their channelized flow in one direction leading to substantial improvement in charge transfer kinetics[24,25] and subdued charge recombination. The increased absorption coefficient[26,27] and reduced carrier scattering rate achieved by means of nanostructuring enhance the PEC performance of the material.[27] To realize higher PEC performance, it is desired for photogenerated charge carriers to participate in the water oxidation process with minimum recombination loss. Time-resolved photoluminescence (TRPL) correlates to charge carrier dynamics and provides average electron−hole pair recombination time.[28,29]

Fabrication of hematite nanostructures can be employed using various techniques such as spray pyrolysis,[30] atmospheric pressure chemical vapor deposition (APCVD),[31] sol−gel,[32,33] hydrothermal,[34,35] anodization,[36,37] and so on. Furthermore, the processes like hydrothermal synthesis,[34,35] anodization,[36,37] electrodeposition,[38] and combustion[39] are efficient techniques to obtain nanosheet-like morphology for the hematite photoanode. The thermal oxidation route used in the present study is a single step, facile, and cost-effective method to synthesize hematite nanostructures,[40−42] does not require rigorous chemical processing, and does not leave behind traces of chemical impurities. Moreover, the resulting nanostructures are single crystalline in nature, which can improve transport of the photogenerated charge carrier and enhance the diffusion length.[43]

Generally, nanostructured iron oxide films are grown on an ITO/FTO substrate for PEC water oxidation, but these are expensive. In contrast, such nanostructures can be grown on a low-cost Fe foil or stainless-steel substrate. PEC studies, however, are barely available on hematite nanostructures grown by the thermal oxidation route and are lacking on 2D structures like nanosheets. In the present investigation, nanosheets have been grown on a piece of pure Fe, and the photocurrent obtained (0.33 mA cm^{-2}) at an applied voltage of 1.23 V_{RHE} is found to be significantly higher than hematite photoanodes fabricated by a similar method.[41,42,44] The reaction kinetics has significant dependence on atomic arrangement on the catalyst surface. α-Fe_2O_3 crystallizes in a corundum structure with a hexagonal lattice having a basal plane (0001). A variety of crystal faces of α-Fe_2O_3 have been studied for their catalytic activity.[45,46] Wu et al. in a theoretical study showed that among (110), (104), and (012) surfaces, the latter offers most favorable oxygen evolution reaction (OER) behavior for water oxidation.[47] The same was observed experimentally by Li et al., where hematite crystallites with the (012) surface were found to have higher OH coverage, which play a positive role in PEC water oxidation reaction.[48] The (0001) surface in hematite is a naturally occurring and thermodynamically stable surface.[49,50] Moreover, the electrical conductivity in the (0001) plane is four times higher than that along [001] direction.[51,52] Both these features of the (0001) surface are advantageous to water splitting.[51] It is worth noting that the α-Fe_2O_3 NSs presented in this work possess the widest surface of (0001). Moreover, the growth is facile with dense coverage under controlled synthesis conditions.

2. EXPERIMENTAL SECTION

Pure Fe pieces (99.97%, Alfa Aesar) were ultrasonicated in acetone, ethanol, and distilled water, respectively, for 10 min each and dried by purging nitrogen. The pieces were placed in an alumina boat and inserted in a quartz tube furnace. The temperature was raised at the rate of 19 °C/min up to 400 °C and held constant for 1 h. After attaining 120 °C during ramping, a moist atmosphere was maintained using a mist generator to enhance the oxidation rate. The sample was left for natural cooling after the heating.

The pulsed laser deposition (PLD) method was used to deposit the thin film of hematite on the FTO substrate to compare its PEC performance with the nanosheet (NS) sample. The target for deposition was prepared by solid state reaction using high purity powder of α-Fe_2O_3 (99.995%, CERAO). The substrate was cleaned before deposition by ultrasonication, following three steps subsequently in acetone, ethanol, and deionized water, each for 10 min. Thin film deposition was carried out for 50 min using a PLD system equipped with a KrF excimer laser (λ = 248 nm), laser repetition rate of 10 Hz, in the presence of 25 mTorr oxygen partial pressure.

Structural characterization was performed by X-ray diffraction (XRD) using an advanced Bruker D8 diffractometer having a Cu K_α (1.54 Å) X-ray source. The data were recorded at an interval of 0.02° in Bragg−Brentano geometry in the 2θ range of 20−70°. Grazing incidence XRD (GIXRD) was recorded using a high-resolution X-ray diffractometer D8 Bruker equipped with a Cu K_α source. The diffraction pattern was recorded at grazing angles (ω) 0.5, 1, 2, and 5°. Field-emission scanning electron microscopy (FESEM) images were recorded to study the morphology and composition of the samples using JEOL, JSM-7610 Plus instrument equipped with an energy dispersive X-ray (EDX) analyzer. Transmission electron microscopy (TEM) images and selective area electron diffraction (SAED) patterns were recorded using a 200 kV TECNAI G^2 20 microscope equipped with a LaB_6 filament and CCD camera. High resolution TEM (HRTEM) images were recorded on FEI model TALOS F200S. X-ray photoelectron spectroscopy (XPS) spectra were recorded on a Surface Nano Analysis GmbH ESCA system, using an Al K_α (1486.6 eV) X-ray source. UV−vis spectra were recorded in diffuse reflection geometry (PerkinElmer, Lambda 950 spectrophotometer) in the spectral range of 200−858 nm. Raman spectra were recorded using a Jobin Yvon Horiba LABRAM HR-800 spectrometer equipped with a CCD detector. Two different laser excitation wavelengths 473 and 633 nm were used to record the spectra. Time-resolved photoluminescence measurements were carried out using a HORIBA Delta Flex time-correlated single photon count (TCSPC) spectrometer, using 288 nm diode as the light source (HORIBA), and HORIBA PPD-850 detector.

PEC measurements were performed on an Autolab PGSTAT-204 electrochemical workstation using a three-electrode electrochemical cell equipped with a quartz window for light incidence. The NS sample was used as the working electrode, Ag/AgCl saturated with 3 M KCl as the reference electrode, and Pt wire as the counter electrode. The electrolyte used was aqueous 1 M NaOH solution with pH 13.3 measured with a pH meter (pH 700, Eutech instruments). The solution was bubbled with N_2 flow for 30 min before measurement to remove any air present in the electrolyte. All surfaces except the front surface of the sample were masked by applying nonconductive Hysol epoxy and allowed to dry in air before immersing into the electrolyte. The working area of the sample was 1.3 cm^2, and the photocurrent obtained was normalized with this area. The working electrode potential used with

https://doi.org/10.1021/acsomega.3c05726
ACS Omega 2023, 8, 38607−38618

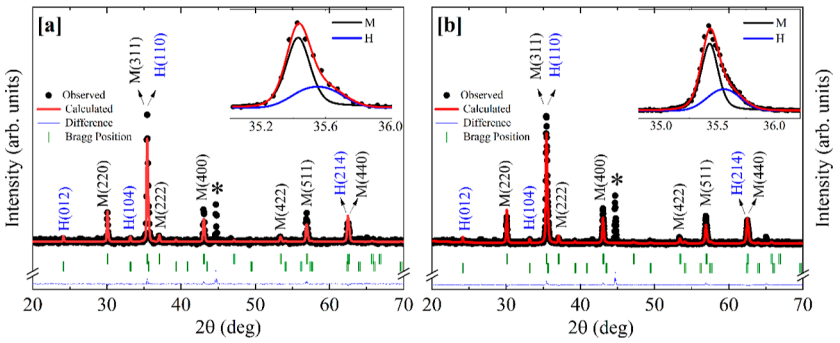

Figure 1. XRD pattern recorded on the NS sample (a) before and (b) after the PEC experiment showing hematite (α-Fe_2O_3) and magnetite (Fe_3O_4) peaks denoted by H and M, respectively. The Fe(110) peak arising from the substrate is marked as "*". The inset shows curve fitting of the peak at 35.5° having overlapping contribution from H and M layers.

reference to Ag/AgCl was converted to reversible hydrogen electrode (RHE) potential using eq 1

$$E_{RHE} = E_{Ag/AgCl} + 0.059 \times pH + 0.197 \quad (1)$$

A high brightness Xe lamp (Holmarc-optomechatronics, HSN Code 9027) was used as the source of incident light on the sample. The power density was 100 mW cm^{-2} measured with a flux meter. Light was illuminated from the front side of the sample surface. Linear sweep voltammetry (LSV) measurement was performed in the potential window from −0.3 to 0.7 V vs Ag/AgCl at a scan rate of 25 mV s^{-1} under dark and chopped light illumination. Mott−Schottky measurement was carried out in light illumination conditions in a potential window from 0.02 to 1.38 V vs RHE with an increment of 0.034 V and frequency set to 1000 Hz, to evaluate the donor density and flat band potential. EIS measurement was performed in a three electrode electrochemical cell in the frequency range of 0.01 Hz to 100 kHz using a modulation signal of 20 mV in the potential window 0.9−1.7 V_{RHE}.

The identification of gaseous products formed as a result of the PEC reaction was performed using a Shimadzu GC-2014 system. The chromatograph was equipped with a shin carbon-ST packed column with a thermal conductivity detector (TCD) using argon as the carrier gas. Parameters were set for the program to detect H_2, and O_2 (detector temperature, 200 °C; oven temperature program, 90 °C (hold time: 1 min), and 90−200 °C (rate: 15 °C per minute) as reported by Kumar et al.[53]

3. RESULTS AND DISCUSSION

3.1. Structural Characterization. Rietveld refinement of the XRD pattern was carried out using the FULLPROF Suite. The diffraction pattern with the calculated profile is shown in Figure 1.

The Rietveld refinement parameters before and after the PEC reaction are listed in Table S1 (Supporting Information). The refinement reveals peaks corresponding predominantly to Fe_3O_4 (magnetite M). The peaks corresponding to α-Fe_2O_3 (hematite H) are visible but have low intensity. The H(110) and M(311) peaks at ∼35° and H(214) and M(440) peaks at ∼62° overlap since reflections of the two phases lie at similar 2θ angles. However, the peak at 35° shows tailing toward higher 2θ, due to the contribution from the H(110) peak, and is shown by peak fitting in the inset Figure 1a,b. It is noted that though the signals of the Fe_3O_4 phase are intense over the α-Fe_2O_3 phase, the most intense peak of α-Fe_2O_3 is clearly seen at 33°, which corresponds to the Bragg position of the (104) peak (JCPDS 74-002). The peak at ∼45° corresponds to the (110) peak of metallic Fe, which is assigned to the signal from the Fe substrate. In order to determine the sequence of the oxide layer formed on the substrate, the GIXRD measurements were performed, which are shown in Figure 2.

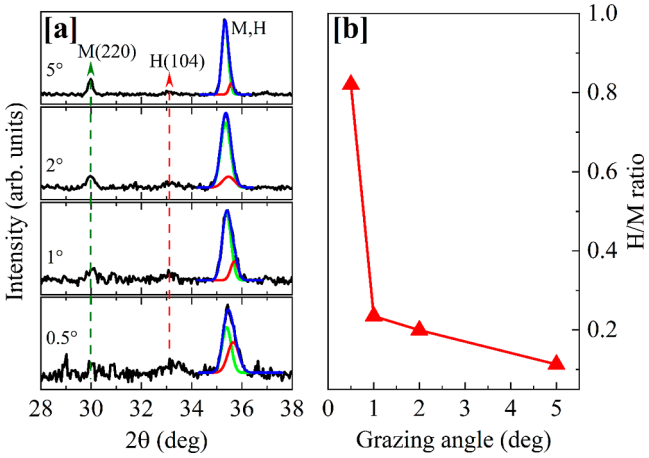

Figure 2. (a) GIXRD pattern recorded on the NS sample at different grazing incidence angles. (b) Peak area obtained from fitting is plotted as ratio H/M against grazing angle. Magnetite and Hematite peaks are denoted as M and H, respectively, in (a,b).

The patterns were recorded from 28 to 38° at different angles of incidence, 0.5, 1, 2, and 5° (Figure 2a). The peak at 35° is fitted for obtaining peak areas under M(311) and H(110) peaks, and the peak area fraction with a grazing angle is plotted in Figure 2b. The area fraction of the H(110) peak is found to decline with the grazing angle, and the drop is rapid from 0.5 to 1°, indicating the presence of a thin hematite layer on magnetite (Figure 2b). The oxide phase FeO is formed when Fe is oxidized above 570 °C.[40,54,55] The synthesis temperature in the present case is 400 °C; hence, no peaks corresponding to the FeO phase were observed in the XRD measurements, and formation of FeO is ruled out. The oxide layer sequence as determined from XRD and GIXRD measurements therefore is α-Fe_2O_3−Fe_3O_4−Fe. Also, the observed oxidization in the sequence Fe to Fe_3O_4 and Fe_3O_4 to α-Fe_2O_3 is consistent with the Ellingham diagram[56] shown in Figure S5 (Supporting Information). Importantly, comparison of the XRD patterns recorded before (Figure 1a) and after PEC (Figure 1b) measurement shows that the intensities of the two phases remain unchanged. This confirms that the iron

https://doi.org/10.1021/acsomega.3c05726
ACS Omega 2023, 8, 38607−38618

oxide layer formed on Fe is stable in an alkaline electrochemical environment. The XRD pattern of the PLD thin film sample (Figure S1 in Supporting Information) shows peaks corresponding to α-Fe_2O_3 and peaks indicated by "*" are from the FTO substrate.

3.2. UV−Vis and Raman Spectroscopy. Estimation of bandgap is crucial as it decides the light absorption characteristic important for the PEC performance of the material. Absorption spectra of the NS sample were studied using UV−vis spectroscopy in diffused reflectance (DR) geometry and compared with that of bulk α-Fe_2O_3 powder as depicted in Figure 3a.

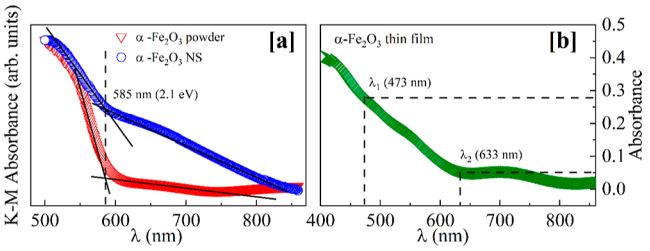

Figure 3. (a) UV−vis diffuse reflectance spectra of the NS sample and bulk α-Fe_2O_3 powder converted to Kubelka−Munk (K−M) absorbance. The vertical dotted line shows the absorption edge at 2.1 eV in both the samples. (b) Absorption spectrum of the α-Fe_2O_3 thin film sample showing absorbance marked at two different wavelengths λ_1 and λ_2 at which the Raman spectra were recorded.

The DR spectra were converted to Kubelka−Munk (K−M) absorption spectra. Both bulk α-Fe_2O_3 powder and the NS sample clearly show absorption edge at 2.1 eV (585 nm), which matches with the band gap of hematite.[57] In the NS sample, below 2.1 eV, the absorption is quite high compared to powder and is attributed to absorption due to the underlying Fe_3O_4 layer having a bandgap of ∼0.2 eV.[58] The penetration depth of light is inversely proportional to the absorption coefficient ($d_p = 1/\alpha$). This infers that the absorption above 2.1 eV arises mainly from the top α-Fe_2O_3 layer of the NS sample. Below the bandgap, absorbance is low, and light penetrates the top α-Fe_2O_3 and enters the Fe_3O_4 layer. This results in increased absorption of light below 2.1 eV arising from the Fe_3O_4 layer in the NS sample.

The UV−vis spectrum was recorded in transmission geometry on the thin film of α-Fe_2O_3 prepared by the PLD method (Figure 3b). The absorbance is marked at two different wavelengths, λ_1 (473 nm) and λ_2 (633 nm), at which the Raman spectra are recorded. The absorbance is 0.28 at 473 nm and 0.05 at 633 nm, which is five times lower. Therefore, at the 633 nm, the light penetrates about five times deeper than at 473 nm, and its consequence on Raman spectra recorded at these two wavelengths is discussed below.

Raman spectroscopy measurements were carried out before and after PEC measurements for comparison, as shown in Figure 4.

There are seven Raman active modes in α-Fe_2O_3 ($2A_{1g} + 5E_g$) that are observed in the spectra recorded on the bulk and NS samples. The A_{1g} modes appear at 227 and 500 cm^{-1}, and E_g modes at 247, 293, 298, 413, and 615 cm^{-1}, which match well with those reported for hematite.[60] The seven Raman modes present below 620 cm^{-1} are zone center phonons with even symmetry. A_{1g} modes involve movement of Fe−O bonds in the zz polarization plane, which are sensitive for properties

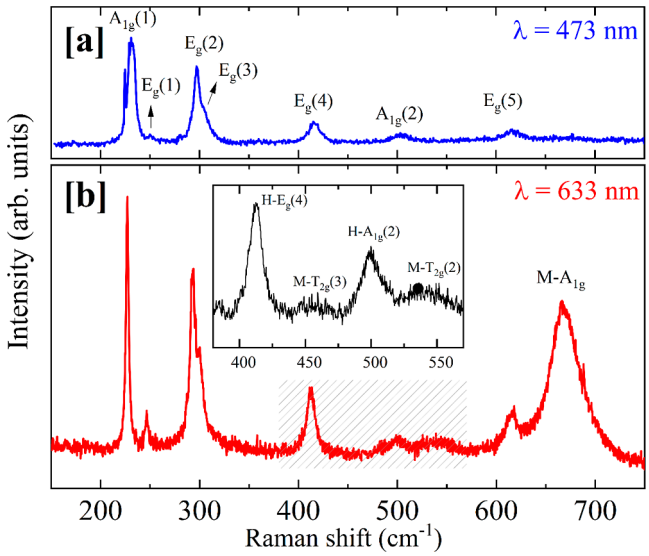

Figure 4. Raman spectra recorded on the NS sample using two different laser wavelengths: (a) 473 and (b) 633 nm. Raman modes of α-Fe_2O_3 (H) are visible in both (a,b). The inset shows the shaded region recorded for longer duration to obtain less intense modes of Fe_3O_4 (M).

along the z axis. The E_g modes are attributed to Fe−O bond vibrations along xz and yz polarization planes.[59,60] The Raman spectra recorded before and after PEC are almost identical, showing that the composition remains unaffected by the PEC reaction. Spectra were recorded at two different laser wavelengths 473 nm (Figure 4a) and 633 nm (Figure 4b) in order to observe the effect of the layered oxide structure on Raman spectra. We recall from the UV−vis results that in the NS sample, light penetrates much deeper at 633 nm than at 473 nm. The spectrum recorded with 633 nm shows an intense peak at 668 cm^{-1}, which is not visible in that recorded with 473 nm. The peak at 668 cm^{-1} belongs to A_{1g} mode of magnetite[61,62] and is attributed to Fe_3O_4 formed below the top layer of hematite. Besides the intense peak at 668 cm^{-1}, two broad peaks of Fe_3O_4 (T_{2g}) centered at 459 and 542 are observed, as shown in the inset of Figure 4b. It may be added that the Raman spectra recorded on the bulk α-Fe_2O_3 pallet using the two wavelengths are very similar (Figure S2 in Supporting Information) unlike those in the NSs sample.

3.3. Morphological Studies. FESEM images recorded on the NS sample are shown in Figure 5. Dense and uniform growth of NSs can be seen in images (Figure 5a,b) recorded at a higher magnification.

The sheets are 100−700 nm across, with an average length of 300 nm evaluated from histogram (Figure S3a in Supporting Information). Elemental composition mapped using energy-dispersive X-ray spectroscopy (EDX) shows peaks pertaining to Fe and O, which confirms formation of iron oxide in the sample (Figure S3b in Supporting Information). The image recorded at the location having sparse coverage (Figure 5c) shows NS having lateral dimensions 100−700 nm, indicating that the growth rate varies at different locations across the sample. The sheets emanate from α-Fe_2O_3 grains that are oriented favorably to facilitate vertical growth of the NSs.[63] It was observed consistently in our synthesis that injection of water vapor promotes formation of NSs to yield dense coverage, whereas in its absence, the growth was sparse (Figure S8 in Supporting Information). The same was observed by

https://doi.org/10.1021/acsomega.3c05726
ACS Omega 2023, 8, 38607−38618

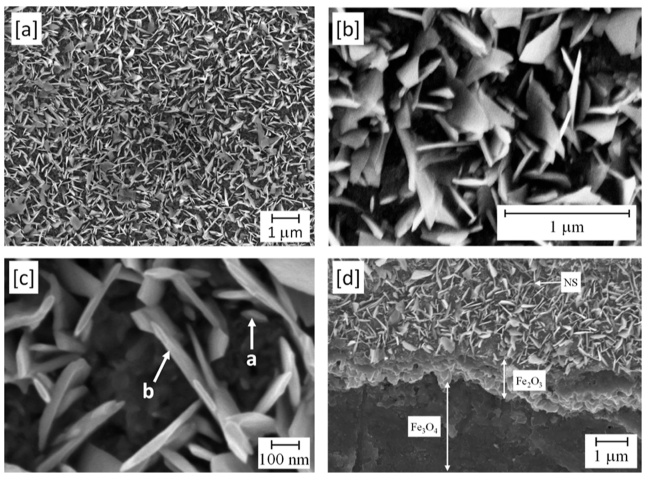

Figure 5. FESEM images of the α-Fe_2O_3 NS sample; (a) low magnification image showing dense and uniform coverage, (b) image showing sheet-like morphology, (c) magnified image showing NSs of varying lateral dimensions from 100 nm marked as "a" and several hundred nm marked as "b", and (d) cross-section image showing distinct morphology α-Fe_2O_3 NSs, layer of α-Fe_2O_3 grains, and the Fe_3O_4 layer in sequence.

several researchers and was attributed to a higher oxidation rate assisted by insertion of protons from dissociated water vapor in the growing oxide layer.[40,54] A cross-sectional image (Figure 5d) shows three morphologically distinct layers, which are ascribed as α-Fe_2O_3 NSs grown on a layer of α-Fe_2O_3 grains, followed by a thick Fe_3O_4 layer that grows on Fe. A porous Fe_3O_4 layer is reported to augment electron transport.[64] It can be seen from Figure S3c in Supporting Information that the underlying Fe_3O_4 layer in the NS sample has a porous structure, which can facilitate transport of photogenerated electrons in the α-Fe_2O_3 NSs to Fe metal at its back contact. The image (Figure S3d in Supporting Information) recorded after the PEC experiment shows the NSs to be intact on the sample surface with no change in their morphology.

TEM measurements were performed to study structural aspects in further detail. The sample surface was gently scraped using a sharp blade, and the NSs were collected on a Cu grid used for TEM investigation. Figure 6a shows a few NSs having lateral dimensions of ~100 nm. The HRTEM image in the inset of Figure 6a shows lattice fringes spaced at 0.256 nm,

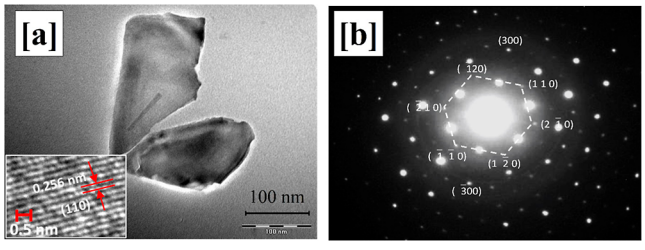

Figure 6. TEM images of α-Fe_2O_3 NSs; (a) transmission image showing NSs having lateral dimensions of ~100 nm. HRTEM image in the inset shows lattice fringes at spacing of 0.256 nm which correspond to (110) planes of the NS (b) SAED pattern with indexed diffraction spots. The zone axis is parallel to the c-axis of the NS. The spots forming vertices of hexagon resulting from hexagonal lattice of α-Fe_2O_3 are shown by a dotted line, except the (300) and $(\bar{3}00)$ spots.

which corresponds to (110) planes of α-Fe_2O_3[65] (also shown in Figure S6 of Supporting Information).

The selected area electron diffraction (SAED) pattern (Figure 6b) shows diffraction spots that reveal the single crystalline nature of the NSs. The pattern was indexed to diffraction planes of α-Fe_2O_3 with the zone axis parallel to c-axis of the NS. The d-spacing calculated from diffraction spots of (300) and (110) reflections 1.45 and 2.52 Å, respectively, matches well with the d-spacing obtained from the XRD pattern. It was verified that the angle between these two spots from the zone axis is 30°, which corresponds to the angle between the (110) and (300) planes. The other indexed diffraction spots arising from set of planes parallel to c-axis, namely, (110), $(2\bar{1}0)$, $(1\bar{2}0)$, $(\bar{1}10)$, $(\bar{2}10)$, and $(\bar{1}20)$ that lie on vertices of a hexagon shown by dotted line in the Figure 6b and are at an angle of 120° between the adjacent planes.

3.4. X-ray Photoelectron Spectroscopy. The semiconductor−electrolyte interface is the site of electrochemical reaction, which infers that the PEC performance is susceptible to changes in the surface properties. Modified surface chemistry due to the sample surface exposed to the electrochemical environment deviates from the PEC performance. The chemical changes taking place on sample surface before and after PEC reaction can be monitored using XPS. The core-level Fe 2p spectra shows spin−orbit doublet Fe $2p_{1/2}$ and Fe $2p_{3/2}$ at 723.9 and 710.4 eV, respectively (Figure 7a).

The feature at ~8 eV on the higher B.E. side of the Fe $2p_{1/2}$ and Fe $2p_{3/2}$ peaks is the Fe^{3+} satellite, which is characteristic of the Fe^{3+} state in α-Fe_2O_3. The Fe 2p spectrum is consistent with that reported on the α-Fe_2O_3 (0001) surface[65] and that of α-Fe_2O_3 nanosheets and nanorods.[66,67] The peak positions of the Fe $2p_{1/2}$ and Fe $2p_{3/2}$ peaks are found to remain unchanged after PEC reaction, as indicated by dotted lines in the figure. The core level O 1s spectra recorded before (Figure 7b) and after (Figure 7c) doing PEC measurements are fitted with three components. Before PEC, the components peak at 529.2, 531.5, and 532.3 eV can be assigned to lattice oxygen in α-Fe_2O_3, hydroxyl group (Fe−OH) on sample surface, and adsorbed water vapor, respectively.[68] The positions of the component peaks after PEC are centered at 529.2, 531.1, and 532.6 eV, respectively. The Fe−O component at 529.2 eV remains intact after PEC, which shows the stability of the lattice oxygen. These XPS results confirm that the α-Fe_2O_3 surface remains chemically stable in the alkaline electrochemical environment.

3.5. Time-Resolved Photoluminescence. The lifetime of photogenerated charge carriers plays a major role in deciding the efficiency of the photoanode material and can be inferred from photoluminescence decay time characteristics. Time-resolved photoluminescence (TRPL) spectra were recorded with the excitation wavelength of 288 nm and emission wavelength of 465 nm for bulk (Figure 8a) and nanosheets (Figure 8b) samples for comparison. We noted from UV−vis spectra that penetration depth of light at lower wavelength (288 nm) is short in α-Fe_2O_3; hence, sole contribution to the PL intensity is attributed to the top layer which is made up of α-Fe_2O_3 NSs in the sample. The measured decay time is related to the charge carrier lifetime, that is, time taken by electron−hole pairs to decay by radiative recombination to $1/e$ of the initial intensity at time t_0. The TRPL data were fitted using the biexponential decay function to obtain the intensity-weighted average decay lifetime $\langle\tau\rangle$.[69] The fitting

https://doi.org/10.1021/acsomega.3c05726
ACS Omega 2023, 8, 38607−38618

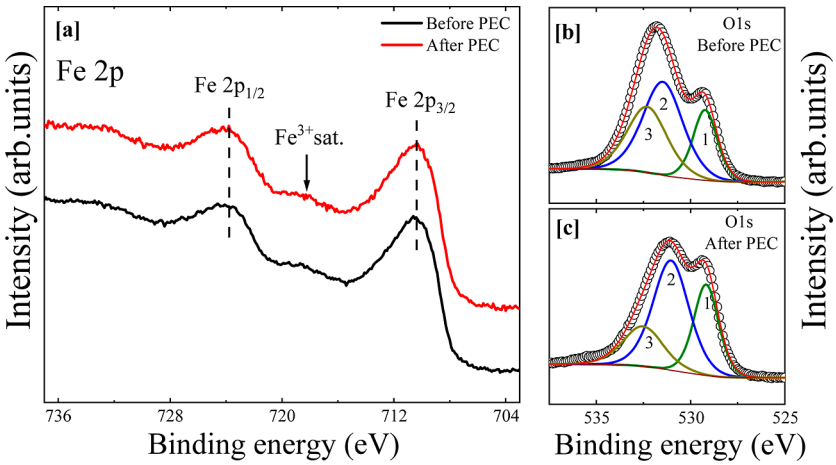

Figure 7. XPS spectra of the NS sample before and after PEC measurements. (a) Fe 2p spectra showing spin−orbit doublet and Fe^{3+} satellite characteristic to α-Fe_2O_3 (b) O 1s spectra recorded before (c) after PEC. Peak labels 1, 2, and 3 indicate Fe−O, Fe−OH, and chemisorbed Fe−OH, respectively.

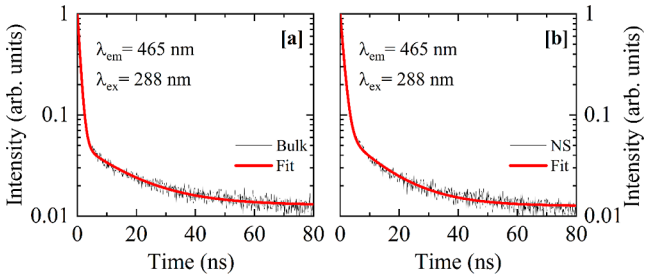

Figure 8. Time-resolved photoluminescence spectra recorded on (a) bulk pallet of α-Fe_2O_3 and (b) α-Fe_2O_3 NS sample at an excitation wavelength (λ_{ex}) of 288 nm and emission wavelength (λ_{em}) measured at 465 nm.

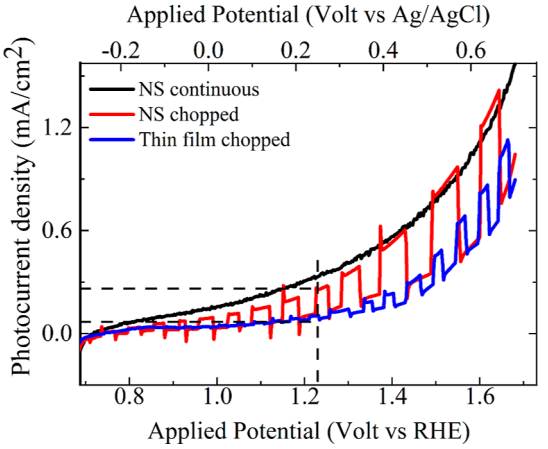

Figure 9. LSV plot of the α-Fe_2O_3 NS and thin film samples shown for comparison. The photocurrent density at 1.23 V_{RHE} in the two samples is indicated by a dotted line.

yields two decay components, which are attributed to multiple recombination routes in the material, and the values obtained are listed (Table S2 in Supporting Information). The average decay lifetime $\langle\tau\rangle$ is found to be 6.1 and 8.9 ns for bulk and NS sample, respectively. The observed decay time values are consistent with the short carrier lifetime known for α-Fe_2O_3.[29] Nevertheless, the 45.9% greater decay time in the NS sample compared to bulk shows delayed recombination. The prolonged lifetime results in increased diffusion length, thereby enhancing the number of holes making their way to NS surface before they recombine and participate in oxidation of water at the interface. Greater lifetime in NSs can be one of the reasons that enhance photocurrent in the NS sample.

3.6. PEC Measurements. Linear sweep voltammetry was performed to evaluate the response of the photoanode under dark and light with continuous and chopped illumination. The measurements were performed on the α-Fe_2O_3 NS sample as well as α-Fe_2O_3 thin film for comparison, as shown in Figure 9.

In the thin film sample, under chopped illumination, the photocurrent density was 0.10 mA/cm^2 at 1.23 V_{RHE}, whereas the NS sample shows photocurrent densities of 0.33 and 0.26 mA/cm^2 under continuous and chopped illumination, respectively, with an applied bias of 1.23 V_{RHE}. It is important to note that the value is 3 times higher in the NS in comparison to the thin film. The reaction products formed during the PEC reaction were analyzed using gas chromatography. The gases evolved in the cell consisted of H_2 and O_2, as shown in Supporting Information (Figure S7). A detailed survey of photocurrent density measured on nanostructures of pristine α-Fe_2O_3 is presented in Table 1.

It can be seen from Table 1 that the synthesis methods employed are rather complex in the literature, where a higher photocurrent of 0.24−0.28 mA/cm^2 is reported.[20,72] In the reports on nanostructures obtained by thermal oxidation of the Fe substrate, the photocurrent density is 0.1−0.2 mA/cm^2 at 1.23 V_{RHE}.[79] Among these, the photocurrent density is 0.19 mA/cm^2 on Fe foil,[44] 0.04 mA/cm^2 on low carbon steel,[41] and 0.18 mA/cm^2 at 1.23 V_{RHE} in thin film grown on the FTO substrate.[42] It is important to note that the photocurrent density of 0.33 mA cm^{-2} at 1.23 V_{RHE} is high among the above-mentioned literature reports where synthesis is simple, cost-effective, and on low-cost substrate.

Upon light illumination, electron−hole pairs are generated in the NSs. Owing to the small thickness of the NSs (a few tens of nanometers), the distance for holes to arrive at the NS surface is small. The small sheet thickness and longer lifetime of photogenerated holes facilitate a larger fraction of holes to be effectively utilized for water oxidation at the NS surface. The NSs possess a large surface area of several μm across and provide a large number of reaction sites. We recall from the SAED pattern in TEM measurements that the widest surface of

https://doi.org/10.1021/acsomega.3c05726
ACS Omega 2023, 8, 38607−38618

Table 1. Subjective Review of Hematite Photoanode Showing Photocurrent $J < J_{NS}$[a]

synthesis method	morphology	substrate	T_a (°C)	J (mA/cm^2)	applied bias (V)	electrolyte	pH	intensity (mW cm^{-2})	remarks	refs
thermal oxidation	nanosheets	pure Fe piece (99.97%)	400	0.33	1.23 V_{RHE}	1 M NaOH	13.3	100		our results
anodization	nanotubes	pure Fe foil (99.5%)	400	0.028	1.4 V_{RHE}	1 M KOH		100	$J < J_{NS}$	70
anodization	nanosphere	iron rods (99.9%)	500	0.078	1.54 V_{RHE}	1 M KOH	14	100	$T_a > T$, $J < J_{NS}$	71
two step anodization	honeycomb film	Fe foil	550	0.24	1.23 V_{RHE}	1 M NaOH	13.6	100	$T_a > T$, $J < J_{NS}$	72
thermal oxidation	nanowire	low carbon steel	620	∼0.04	0.5 vs SCE	1 M NaOH		75 W lamp	$T_a > T$, $J < J_{NS}$	41
sol gel	nanoparticles	FTO	500	∼0.07	0.8 vs NHE	1 M KOH		400	$T_a > T$, $J < J_{NS}$	32
aqueous chemical growth	nanorod	FTO	450	∼0.034	1.23 V_{RHE}	0.5 M Na_2SO_4	7	100	$T_a > T$, $J < J_{NS}$	73
thermal air oxidation followed by sputtering	granular particles	FTO	255	0.18	0.23 V vs Ag/AgCl	1 M NaOH		100	$J < J_{NS}$	42
PLD	granular particles	FTO		0.48	1.48 V_{RHE}	1 M NaOH	13.6	100	$J < J_{NS}$	74
hydrothermal	nanoparticles	FTO	100	0.21	1.23 V_{RHE}	1 M NaOH + 0.5 M H_2O_2		100	$J < J_{NS}$	75
dip coating	dendrites	ITO	500	0.018	1.23 V_{RHE}	1 M NaOH		100	$T_a > T$, $J < J_{NS}$	76
anodization	nanorod	FTO	450	0.05	1.23 V_{RHE}	1 M KOH	13.6	100	$T_a > T$, $J < J_{NS}$	36
hydrothermal	nanowires	FTO	550	0.035	1.23 V_{RHE}	1 M NaOH	13.6	100	$T_a > T$, $J < J_{NS}$	77
air annealing	nanorods	Fe foil	450	∼0.19	1.23 V_{RHE}	1 M KOH		100	$T_a > T$, $J < J_{NS}$	44
chemical vapor deposition	spindle-like grains	FTO		∼0.28	1.23 V_{RHE}	1 M NaOH	13.6	100	$T_a > T$, $J < J_{NS}$	20
anodic oxidation	pure hematite nanotubes	Fe foil	500	0.75	1.6 V_{RHE}	1 M NaOH	13.6	100	$T_a > T$, $J > J_{NS}$	21
anodization	nonporous film	Fe foil	450	0.13	0.5 vs Ag/AgCl	1 M NaOH		100	$T_a > T$, $J < J_{NS}$	78

[a] T_a: annealing temperature; J: photocurrent density, T: annealing temperature for NS sample (400 °C), ∼ stands for approximately values.

https://doi.org/10.1021/acsomega.3c05726
ACS Omega 2023, 8, 38607−38618

the NS is (0001), which is basal plane of α-Fe_2O_3. The (0001) surface is naturally occurring and thermodynamically most stable for photo-oxidation of water.[49,50] The (0001) plane of α-Fe_2O_3 has larger packing density of Fe^{3+} and O^{2-} ions which participate in the reaction.[80] The proportion of the (0001) plane in nanosheet is almost 100%; on the other hand, that in nanorod is about 23%.[80] Also, the electronic conduction in the basal plane (0001) is 4 orders of magnitude higher than that in the perpendicular planes.[81,82] Superior conductivity in the (0001) plane can facilitate the transport of photogenerated charge carriers. Dense growth of the NSs offers a large area of the (0001) surface for water oxidation. Photogenerated holes can hop between the (0001) planes to reach the electrolyte interface and participate in water oxidation reaction to yield efficient PEC performance.[81,83,84] A downside is that the overall electrical conductivity of α-Fe_2O_3 is low, of the order of 10^{-11} S cm^{-1}.[85] On the other hand, the conductivity of Fe_3O_4 is high, about 250 S cm^{-1}.[86,87] Higher electrical conductivity of the underlying Fe_3O_4 layer in the NS sample can facilitate efficient transport of photogenerated electrons from the top α-Fe_2O_3 NS layer to the back contact, which is Fe metal, whereby they reach the platinum counter electrode. These factors can collectively enhance the oxidation of water on the NS surface and are attributed to observed higher photocurrent in the present study.

In order to investigate the effect of nanostructuring on electrochemical properties, Mott–Schottky (M-S) measurements were performed in 1 M aqueous NaOH solution. The flat band potential and carrier density was estimated using Mott–Schottky (M–S) eq 2[88,89]

$$\frac{1}{C^2} = \frac{2}{qA^2\varepsilon\varepsilon_0 N_D}\left(V - V_{FB} - \frac{K_B T}{q}\right) \quad (2)$$

Here, C is specific capacitance (F/cm^2), q is elementary charge (1.6×10^{-19}C), A is the semiconductor–electrolyte contact area (cm^2), ε = 80 is relative permittivity of hematite photoanode,[90] ε_0 is vacuum permittivity (8.854×10^{-12} F m^{-1}), N_D is donor density (cm^{-3}), V is applied potential (volts), V_{FB} is flat band potential, K_B is the Boltzmann constant [1.38×10^{-23} J K^{-1}], and T is the absolute temperature (K).

According to eq 2, the flat band potential (V_{FB}) can be obtained from the x-intercept of the linear region of the Mott–Schottky curve, and the donor density (N_D) from slope of linear part of the curve, using eq 3[89]

$$N_D = \left(\frac{2}{q\varepsilon\varepsilon_0}\right)\left[\frac{d(1/C^2)}{dV}\right]^{-1} \quad (3)$$

Both NS and thin film samples show a positive slope (Figure 10a), which indicates n-type conductivity of the samples.[91,92] The calculated flat band potential values are 0.65 and 0.47 V_{RHE}, and the donor densities are 9.59×10^{17} and 1.85×10^{18} cm^{-3}, for NS and thin film samples, respectively. These values are consistent with the reports on hematite photoanodes.[77,93,94]

In general, for a photoanode material to have better PEC performance, it is advantageous to have the V_{FB} shifting anodically with higher donor density to achieve greater OER activity. The parameters V_{FB} and N_D are related to surface states and charge transport characteristics, respectively.[89,95] It is found that the calculated donor densities are within the same order of magnitude ($\sim 10^{18}$ cm^{-3}) in both the samples. The flat band potential exhibits a noticeable increase of 38.3% in the NS sample compared to that of the thin film. This can be one of the contributing factors for observed three-fold increase in the photocurrent density in the NS sample.

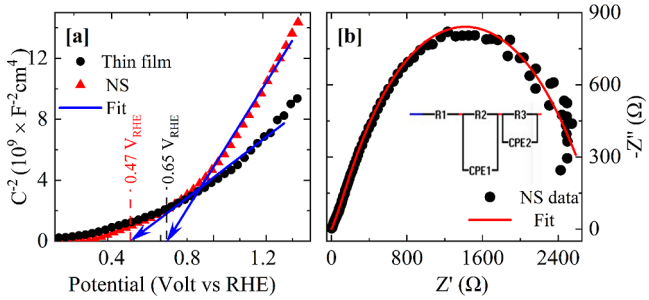

Figure 10. (a) Mott–Schottky plot showing n-type conductivity for both NSs and bulk α-Fe_2O_3; the intercept on x-axis indicates the value of flat band potential V_{FB}. (b) Nyquist plot for the NS sample fitted with the equivalent circuit model.

Electrochemical impedance spectroscopy (EIS) analysis was performed in order to get further insights into a possible mechanism for the observed enhancement in photocurrent density of the NS sample in comparison to the thin film. It is clear (Figure S4 in Supporting Information) that the semicircle for the NS sample is smaller than that of thin film, displaying enhancement in charge carrier separation and transport. The EIS data of the NS sample were fitted by an equivalent circuit model using EIS spectrum analyzer software. The circuit was best fitted to a 2-RQ circuit model (Figure 10b), which consists of one resistor and two RQ circuits in series, each having a resistor and constant phase element in parallel, similar to that used in refs 30 and 43. The two RQ circuits presented in the model can be ascribed mainly to the two interfaces, NS-electrolyte and bulk hematite, developing the impedance elements.[96,97] The observed larger charge transfer resistance (R_{ct}) and double layer capacitance (Q_{dl}) can lead to a sluggish water oxidation reaction that takes place at the photoanode-electrolyte interface. The space charge resistance and capacitance (R_{sc} and Q_{sc}) arise from events occurring at the bulk semiconductor. The values for the equivalent circuit fitting parameters are listed (Table S3 in Supporting Information). The EIS result shows improved charge carrier dynamics and the charge transport. It is further noted that the interfacial processers are affected by the crystallographic orientation of the electrode and have implications on the charge carrier dynamics and subsequent water oxidation reaction.[98−101] In the presence of aqueous electrolyte, the (0001) surface of hematite gets hydroxylated. The H bonding interactions between the interfacial water molecules and hematite lead to hydrophilic character of the surface. These connected hydroxyl groups are proton-active, which participate actively to enhance OER activity of the reaction.[98,102,103]

4. CONCLUSIONS

To conclude, dense arrays of single crystalline α-Fe_2O_3 nanosheets were grown by simple heating of Fe in moist atmosphere for 1 h, and it shows a three times higher photocurrent than that of a thin film deposited on the expensive FTO substrate. The NSs have the widest surface along the basal plane (0001) of α-Fe_2O_3, which is thermodynamically stable, having high electrical conductivity reported elsewhere. Densely grown NSs with a (0001) surface

https://doi.org/10.1021/acsomega.3c05726
ACS Omega 2023, 8, 38607−38618

provide a large number of sites for PEC reaction. A higher lifetime of photogenerated charge carriers, anodically shifted flat-band potential, and lower charge transfer resistance are factors that enhance the photocurrent. The greater PEC performance of the NS photoanode is attributed to all these factors adding up favorably. The NS morphology and chemical composition are found to remain unchanged after PEC. These results endorse the suitability of the hematite NS photoanode for PEC water splitting application. In this study, higher PEC performance has been achieved by a simple, single-step, and low-cost synthesis.[103]

■ ASSOCIATED CONTENT

Supporting Information

The Supporting Information is available free of charge at https://pubs.acs.org/doi/10.1021/acsomega.3c05726.

Thin film XRD patterns, Raman spectrum of bulk α-Fe_2O_3 pallet, FESEM, EDX and histogram for NS sample and raw EIS data for both NS and thin film sample, Ellingham diagram, HRTEM image, GC-TCD analysis of gases evolved, SEM image of NSs in the absence of water vapor, XRD fitting parameters, TRPL decay time parameters, and EIS fitting parameters (PDF)

■ AUTHOR INFORMATION

Corresponding Author

Uday Deshpande − *UGC-DAE Consortium for Scientific Research, Indore 452001 Madhya Pradesh, India*; Email: uday@csr.res.in

Authors

Parveen Garg − *UGC-DAE Consortium for Scientific Research, Indore 452001 Madhya Pradesh, India*; orcid.org/0000-0002-8046-3288

Lokanath Mohapatra − *Department of Metallurgical Engineering and Materials Science, Indian Institute of Technology Indore, Simrol, Indore 453552, India*

Ajay Kumar Poonia − *Department of Physics, Indian Institute of Science Education and Research Bhopal, Bhopal 462066, India*; orcid.org/0000-0002-5551-7299

Ajay Kumar Kushwaha − *Department of Metallurgical Engineering and Materials Science, Indian Institute of Technology Indore, Simrol, Indore 453552, India*

Kumaran Nair Valsala Devi Adarsh − *Department of Physics, Indian Institute of Science Education and Research Bhopal, Bhopal 462066, India*; orcid.org/0000-0002-6337-6545

Complete contact information is available at: https://pubs.acs.org/10.1021/acsomega.3c05726

Author Contributions

Parveen Garg: conceptualization, methodology, formal analysis, investigation, writing—original draft. Lokanath Mohapatra: resources. Uday Deshpande: writing—reviewing and editing, supervision.

Funding

UGC-DAE Consortium for Scientific Research, University Campus, Khandwa Road, Indore-452001, Madhya Pradesh, India.

Notes

The authors declare no competing financial interest.

■ ACKNOWLEDGMENTS

Authors acknowledge Layanta Behera and Mukul Gupta for providing the XRD pattern; A. Gome and V. R. Reddy for GIXRD measurement; Ajay Rathore and V. G. Sathe for Raman measurements; Sachin Kumar for UV−vis and XPS measurements; Manoj Kumar and R. J. Choudhary for PLD thin film deposition; and Preeti Mahajan and N. P. Lalla for providing TEM measurements. Pramod R. Nadig and Lozil Denzil Mendonca are acknowledged for providing their valuable suggestions. Dr. Sanjay Kumar Singh and Ankit Kumar, IIT Indore, provided the GC measurements. The authors also acknowledge the FIST facility, Department of Chemistry, IISER Bhopal for HRTEM measurements.

■ ABBREVIATIONS

PEC, photoelectrochemical; OER, Oxygen evolution reaction; NS, nanosheets

■ REFERENCES

(1) Dincer, I.; Acar, C. Review and Evaluation of Hydrogen Production Methods for Better Sustainability. *Int. J. Hydrogen Energy* **2015**, *40* (34), 11094−11111.

(2) Fujishima, A.; Honda, K. Electrochemical Photolysis of Water at a Semiconductor Electrode. *Nature* **1972**, *238* (5358), 37−38.

(3) Hardee, K. L.; Bard, A. J. Semiconductor Electrodes: V. The Application of Chemically Vapor Deposited Iron Oxide Films to Photosensitized Electrolysis. *J. Electrochem. Soc.* **1976**, *123* (7), 1024−1026.

(4) Sgarbi, R.; Kumar, K.; Saveleva, V. A.; Dubau, L.; Chattot, R.; Martin, V.; Mermoux, M.; Bordet, P.; Glatzel, P.; Ticianelli, E. A.; Jaouen, F.; Maillard, F. Electrochemical Transformation of Fe-N-C Catalysts into Iron Oxides in Alkaline Medium and Its Impact on the Oxygen Reduction Reaction Activity. *Appl. Catal., B* **2022**, *311*, 121366.

(5) Chan, J. Y. T.; Ang, S. Y.; Ye, E. Y.; Sullivan, M.; Zhang, J.; Lin, M. Heterogeneous Photo-Fenton Reaction on Hematite (α-Fe $_2$ O $_3$){104}, {113} and {001} Surface Facets. *Phys. Chem. Chem. Phys.* **2015**, *17* (38), 25333−25341.

(6) Tanaka, S.; Kaneti, Y. V.; Septiani, N. L. W.; Dou, S. X.; Bando, Y.; Hossain, M. S. A.; Kim, J.; Yamauchi, Y. A Review on Iron Oxide-Based Nanoarchitectures for Biomedical, Energy Storage, and Environmental Applications. *Small Methods* **2019**, *3* (5), 1800512.

(7) Muraro, P. C. L.; Mortari, S. R.; Vizzotto, B. S.; Chuy, G.; dos Santos, C.; Brum, L. F. W.; da Silva, W. L. Iron Oxide Nanocatalyst with Titanium and Silver Nanoparticles: Synthesis, Characterization and Photocatalytic Activity on the Degradation of Rhodamine B Dye. *Sci. Rep.* **2020**, *10* (1), 3055.

(8) Kaneti, Y. V.; Zakaria, Q. M. D.; Zhang, Z.; Chen, C.; Yue, J.; Liu, M.; Jiang, X.; Yu, A. Solvothermal Synthesis of ZnO-Decorated α-Fe $_2$ O $_3$ Nanorods with Highly Enhanced Gas-Sensing Performance toward n-Butanol. *J. Mater. Chem. A* **2014**, *2* (33), 13283−13292.

(9) Kaneti, Y. V.; Moriceau, J.; Liu, M.; Yuan, Y.; Zakaria, Q.; Jiang, X.; Yu, A. Hydrothermal synthesis of ternary α-Fe2O3−ZnO−Au nanocomposites with high gas-sensing performance. *Sens. Actuators, B* **2015**, *209*, 889−897.

(10) Ling, Y.; Wang, G.; Wheeler, D. A.; Zhang, J. Z.; Li, Y. Sn-Doped Hematite Nanostructures for Photoelectrochemical Water Splitting. *Nano Lett.* **2011**, *11* (5), 2119−2125.

(11) Kment, S.; Schmuki, P.; Hubicka, Z.; Machala, L.; Kirchgeorg, R.; Liu, N.; Wang, L.; Lee, K.; Olejnicek, J.; Cada, M.; Gregora, I.; Zboril, R. Photoanodes with Fully Controllable Texture: The Enhanced Water Splitting Efficiency of Thin Hematite Films Exhibiting Solely (110) Crystal Orientation. *ACS Nano* **2015**, *9* (7), 7113−7123.

(12) Tamirat, A. G.; Rick, J.; Dubale, A. A.; Su, W.-N.; Hwang, B.-J. Using Hematite for Photoelectrochemical Water Splitting: A Review

of Current Progress and Challenges. *Nanoscale Horiz.* **2016**, *1* (4), 243−267.
(13) Biswas, P.; Ainabayev, A.; Zhussupbekova, A.; Jose, F.; O'Connor, R.; Kaisha, A.; Walls, B.; Shvets, I. V. Tuning of Oxygen Vacancy-Induced Electrical Conductivity in Ti-Doped Hematite Films and Its Impact on Photoelectrochemical Water Splitting. *Sci. Rep.* **2020**, *10* (1), 7463.
(14) Morin, F. J. Electrical Properties of α Fe 2 O 3 and α Fe 2 O 3 Containing Titanium. *Phys. Rev.* **1951**, *83* (5), 1005−1010.
(15) Tilley, S. D.; Cornuz, M.; Sivula, K.; Grätzel, M. Light-Induced Water Splitting with Hematite: Improved Nanostructure and Iridium Oxide Catalysis. *Angew. Chem., Int. Ed.* **2010**, *49* (36), 6405−6408.
(16) Sivula, K.; Zboril, R.; Le Formal, F.; Robert, R.; Weidenkaff, A.; Tucek, J.; Frydrych, J.; Grätzel, M. Photoelectrochemical Water Splitting with Mesoporous Hematite Prepared by a Solution-Based Colloidal Approach. *J. Am. Chem. Soc.* **2010**, *132* (21), 7436−7444.
(17) Ahart, C. S.; Rosso, K. M.; Blumberger, J. Electron and Hole Mobilities in Bulk Hematite from Spin-Constrained Density Functional Theory. *J. Am. Chem. Soc.* **2022**, *144* (10), 4623−4632.
(18) Ahn, H.-J.; Yoon, K.-Y.; Kwak, M.-J.; Jang, J.-H. A Titanium-Doped SiO_x Passivation Layer for Greatly Enhanced Performance of a Hematite-Based Photoelectrochemical System. *Angew. Chem.* **2016**, *128* (34), 10076−10080.
(19) Ahmed, M. G.; Zhang, M.; Tay, Y. F.; Chiam, S. Y.; Wong, L. H. Surface Modification of Hematite Photoanodes with CeO_x Cocatalyst for Improved Photoelectrochemical Water Oxidation Kinetics. *ChemSusChem* **2020**, *13* (20), 5489−5496.
(20) Leduc, J.; Goenuellue, Y.; Ghamgosar, P.; You, S.; Mouzon, J.; Choi, H.; Vomiero, A.; Grosch, M.; Mathur, S. Electronically-Coupled Phase Boundaries in α-Fe_2O_3/Fe_3O_4 Nanocomposite Photoanodes for Enhanced Water Oxidation. *ACS Appl. Nano Mater.* **2019**, *2* (1), 334−342.
(21) Xue, J.; Zhang, N.; Shen, Q.; Li, Q.; Liu, X.; Jia, H.; Guan, R. In-Situ Construction of Photoanode with Fe2O3/Fe3O4 Heterojunction Nanotube Array to Facilitate Charge Separation for Efficient Water Splitting. *J. Alloys Compd.* **2022**, *918*, 165787.
(22) Wheeler, D. A.; Wang, G.; Ling, Y.; Li, Y.; Zhang, J. Z. Nanostructured Hematite: Synthesis, Characterization, Charge Carrier Dynamics, and Photoelectrochemical Properties. *Energy Environ. Sci.* **2012**, *5* (5), 6682.
(23) Joy, J.; Mathew, J.; George, S. C. Nanomaterials for Photoelectrochemical Water Splitting - Review. *Int. J. Hydrogen Energy* **2018**, *43* (10), 4804−4817.
(24) Shen, S.; Kronawitter, C. X.; Jiang, J.; Mao, S. S.; Guo, L. Surface Tuning for Promoted Charge Transfer in Hematite Nanorod Arrays as Water-Splitting Photoanodes. *Nano Res.* **2012**, *5* (5), 327−336.
(25) Lei, W.; Yu, Y.; Zhang, H.; Jia, Q.; Zhang, S. Defect Engineering of Nanostructures: Insights into Photoelectrochemical Water Splitting. *Mater. Today* **2022**, *52*, 133−160.
(26) Edman Jonsson, G.; Fredriksson, H.; Sellappan, R.; Chakarov, D. Nanostructures for Enhanced Light Absorption in Solar Energy Devices. *Int. J. Photoenergy* **2011**, *2011*, 1−11.
(27) Li, Y.; Zhang, J. z. Hydrogen Generation from Photoelectrochemical Water Splitting Based on Nanomaterials. *Laser Photon. Rev.* **2009**, *4* (4), 517−528.
(28) Hjiri, M.; Alonizan, N. H.; Althubayti, M. M.; Alshammari, S.; Besbes, H.; Aida, M. S. Preparation and Photoluminescence of NiFe2O4 Nanoparticles. *J. Mater. Sci.: Mater. Electron.* **2019**, *30* (16), 15379−15387.
(29) Yang, G.; Li, Y.; Lin, H.; Ren, X.; Philo, D.; Wang, Q.; He, Y.; Ichihara, F.; Luo, S.; Wang, S.; Ye, J. Constructing Chemical Interaction between Hematite and Carbon Nanosheets with Single Active Sites for Efficient Photo-Electrochemical Water Oxidation. *Small Methods* **2020**, *4* (12), 2000577.
(30) Lopes, T.; Andrade, L.; Le Formal, F.; Gratzel, M.; Sivula, K.; Mendes, A. Hematite Photoelectrodes for Water Splitting: Evaluation of the Role of Film Thickness by Impedance Spectroscopy. *Phys. Chem. Chem. Phys.* **2014**, *16* (31), 16515.
(31) Zhang, P.; Kleiman-Shwarsctein, A.; Hu, Y.-S.; Lefton, J.; Sharma, S.; Forman, A. J.; McFarland, E. Oriented Ti Doped Hematite Thin Film as Active Photoanodes Synthesized by Facile APCVD. *Energy Environ. Sci.* **2011**, *4* (3), 1020−1028.
(32) Herrmann-Geppert, I.; Bogdanoff, P.; Radnik, J.; Fengler, S.; Dittrich, T.; Fiechter, S. Surface Aspects of Sol-Gel Derived Hematite Films for the Photoelectrochemical Oxidation of Water. *Phys. Chem. Chem. Phys.* **2013**, *15* (5), 1389−1398.
(33) Lian, X.; Yang, X.; Liu, S.; Xu, Y.; Jiang, C.; Chen, J.; Wang, R. Enhanced Photoelectrochemical Performance of Ti-Doped Hematite Thin Films Prepared by the Sol-Gel Method. *Appl. Surf. Sci.* **2012**, *258* (7), 2307−2311.
(34) Ji, M.; Cai, J.; Ma, Y.; Qi, L. Controlled Growth of Ferrihydrite Branched Nanosheet Arrays and Their Transformation to Hematite Nanosheet Arrays for Photoelectrochemical Water Splitting. *ACS Appl. Mater. Interfaces* **2016**, *8* (6), 3651−3660.
(35) Zhao, L.; Xiao, J.; Huang, H.; Huang, Q.; Zhao, Y.; Li, Y. Enhanced Efficiency of Hematite Photoanode for Water Splitting with the Doping of Ge. *Int. J. Hydrogen Energy* **2018**, *43* (28), 12646−12652.
(36) Fu, L.; Yu, H.; Li, Y.; Zhang, C.; Wang, X.; Shao, Z.; Yi, B. Ethylene Glycol Adjusted Nanorod Hematite Film for Active Photoelectrochemical Water Splitting. *Phys. Chem. Chem. Phys.* **2014**, *16* (9), 4284.
(37) Peerakiatkhajohn, P.; Yun, J.; Chen, H.; Lyu, M.; Butburee, T.; Wang, L. Stable Hematite Nanosheet Photoanodes for Enhanced Photoelectrochemical Water Splitting. *Adv. Mater.* **2016**, *28* (30), 6405−6410.
(38) Li, L.; Zhang, H.; Liu, C.; Liang, P.; Mitsuzaki, N.; Chen, Z. The Effect of Annealing Regime and Electrodeposition Time on Morphology and Photoelecrochemical Performance of Hematite Converted from Nanosheet γ-FeOOH. *J. Photochem. Photobiol., A* **2019**, *369*, 8−15.
(39) Huang, M.; Qin, M.; Chen, P.; Jia, B.; Chen, Z.; Li, R.; Liu, Z.; Qu, X. Facile preparation of network-like porous hematite (α-Fe 2 O 3) nanosheets via a novel combustion-based route. *Ceram. Int.* **2016**, *42* (8), 10380−10388.
(40) Budiman, F.; Kian, T. W.; Razak, K. A.; Matsuda, A.; Lockman, Z. The Assessment of Cr(VI) Removal by Iron Oxide Nanosheets and Nanowires Synthesized by Thermal Oxidation of Iron in Water Vapour. *Procedia Chem.* **2016**, *19*, 586−593.
(41) Dlugosch, T.; Chnani, A.; Muralidhar, P.; Schirmer, A.; Biskupek, J.; Strehle, S. Thermal Oxidation Synthesis of Crystalline Iron-Oxide Nanowires on Low-Cost Steel Substrates for Solar Water Splitting. *Semicond. Sci. Technol.* **2017**, *32* (8), 084001.
(42) Hiralal, P.; Saremi-Yarahmadi, S.; Bayer, B. C.; Wang, H.; Hofmann, S.; Upul Wijayantha, K. G.; Amaratunga, G. A. J. Nanostructured Hematite Photoelectrochemical Electrodes Prepared by the Low Temperature Thermal Oxidation of Iron. *Sol. Energy Mater. Sol. Cells* **2011**, *95* (7), 1819−1825.
(43) Kim, J. Y.; Magesh, G.; Youn, D. H.; Jang, J.-W.; Kubota, J.; Domen, K.; Lee, J. S. Single-Crystalline, Wormlike Hematite Photoanodes for Efficient Solar Water Splitting. *Sci. Rep.* **2013**, *3* (1), 2681.
(44) Lei, B.; Xu, D.; Wei, B.; Xie, T.; Xiao, C.; Jin, W.; Xu, L. In Situ Synthesis of α-Fe_2O_3/Fe_3O_4 Heterojunction Photoanode via Fast Flame Annealing for Enhanced Charge Separation and Water Oxidation. *ACS Appl. Mater. Interfaces* **2021**, *13* (3), 4785−4795.
(45) Sun, L.; Zhan, W.; Li, Y.-A.; Wang, F.; Zhang, X.; Han, X. Understanding the Facet-Dependent Catalytic Performance of Hematite Microcrystals in a CO Oxidation Reaction. *Inorg. Chem. Front.* **2018**, *5* (9), 2332−2339.
(46) Rehman, S.; Yang, W.; Liu, F.; Hong, Y.; Wang, T.; Hou, Y. Facile Synthesis of Anisotropic Single Crystalline α-Fe_2O_3 Nanoplates and Their Facet-Dependent Catalytic Performance. *Inorg. Chem. Front.* **2015**, *2* (6), 576−583.
(47) Wu, H.; Yang, T.; Du, Y.; Shen, L.; Ho, G. W. Identification of Facet-Governing Reactivity in Hematite for Oxygen Evolution. *Adv. Mater.* **2018**, *30* (52), 1804341.

https://doi.org/10.1021/acsomega.3c05726
ACS Omega 2023, 8, 38607−38618

(48) Li, W.; Yang, K. R.; Yao, X.; He, Y.; Dong, Q.; Brudvig, G. W.; Batista, V. S.; Wang, D. Facet-Dependent Kinetics and Energetics of Hematite for Solar Water Oxidation Reactions. *ACS Appl. Mater. Interfaces* **2019**, *11* (6), 5616−5622.
(49) Wang, X.-G.; Weiss, W.; Shaikhutdinov, Sh. K.; Ritter, M.; Petersen, M.; Wagner, F.; Schlögl, R.; Scheffler, M. The Hematite (α-Fe2O3) (0001) Surface: Evidence for Domains of Distinct Chemistry. *Phys. Rev. Lett.* **1998**, *81* (5), 1038−1041.
(50) Nguyen, M.-T.; Piccinin, S.; Seriani, N.; Gebauer, R. Photo-Oxidation of Water on Defective Hematite(0001). *ACS Catal.* **2015**, *5* (2), 715−721.
(51) Pan, H.; Meng, X.; Qin, G. Hydrogen Generation by Water Splitting on Hematite (0001) Surfaces: First-Principles Calculations. *Phys. Chem. Chem. Phys.* **2014**, *16* (46), 25442−25448.
(52) Pabisiak, T.; Kiejna, A. Incipient Adsorption of Water and Hydroxyl on Hematite (0001) Surface. *J. Phys. Commun.* **2019**, *3* (3), 035023.
(53) Kumar, A.; Awasthi, M. K.; Sheet, N.; Kharde, T. A.; Singh, S. K. One-pot Upcycling of Waste Plastics for Selective Hydrogen Production at Low-Temperature. *ChemCatChem* **2023**, *15*, No. e202300574.
(54) Pujilaksono, B.; Jonsson, T.; Halvarsson, M.; Svensson, J.-E.; Johansson, L.-G. Oxidation of Iron at 400−600°C in Dry and Wet O2. *Corros. Sci.* **2010**, *52* (5), 1560−1569.
(55) Yuan, J.; Wang, W.; Zhu, S.; Wang, F. Comparison between the Oxidation of Iron in Oxygen and in Steam at 650−750°C. *Corros. Sci.* **2013**, *75*, 309−317.
(56) Gaskell, D. R. Metal Production: Ellingham Diagrams. *Encyclopedia of Materials: Science and Technology*; Elsevier, 2001; pp 5481−5486.
(57) Xia, C.; Jia, Y.; Tao, M.; Zhang, Q. Tuning the band gap of hematite α-Fe2O3 by sulfur doping. *Phys. Lett. A* **2013**, *377* (31−33), 1943−1947.
(58) Liu, H.; Di Valentin, C. Band Gap in Magnetite above Verwey Temperature Induced by Symmetry Breaking. *J. Phys. Chem. C* **2017**, *121* (46), 25736−25742.
(59) Zong, M.; Zhang, X.; Wang, Y.; Huang, X.; Zhou, J.; Wang, Z.; De Yoreo, J. J.; Lu, X.; Rosso, K. M. Synthesis of 2D Hexagonal Hematite Nanosheets and the Crystal Growth Mechanism. *Inorg. Chem.* **2019**, *58* (24), 16727−16735.
(60) Beattie, I. R.; Gilson, T. R. The Single-Crystal Raman Spectra of Nearly Opaque Materials. Iron(III) Oxide and Chromium(III) Oxide. *J. Chem. Soc. A* **1970**, 980−986.
(61) Shebanova, O. N.; Lazor, P. Raman Spectroscopic Study of Magnetite (FeFe2O4): A New Assignment for the Vibrational Spectrum. *J. Solid State Chem.* **2003**, *174* (2), 424−430.
(62) Zhong, M.; Liu, Z.; Yu, H.; Zhong, X.; Zeng, D.; Ramanujan, R. V. Low-Temperature Synthesis and Nanomagnetism of Large-Area <I>α</I>-Fe₂O₃ Nanobelts. *J. Nanosci. Nanotechnol.* **2013**, *13* (2), 1525−1529.
(63) Yuan, L.; Cai, R.; Jang, J. I.; Zhu, W.; Wang, C.; Wang, Y.; Zhou, G. Morphological Transformation of Hematite Nanostructures during Oxidation of Iron. *Nanoscale* **2013**, *5* (16), 7581.
(64) Cui, X.; Liu, T.; Zhang, Z.; Wang, L.; Zuo, S.; Zhu, W. Hematite Nanorods with Tunable Porous Structure: Facile Hydrothermal-Calcination Route Synthesis, Optical and Photocatalytic Properties. *Powder Technol.* **2014**, *266*, 113−119.
(65) Wu, J.; Chen, J.; Deng, S.; Xu, N. P2−16: Field Emission Properties of α-Fe2O3 Nanostructures Prepared from Iron Thin Film with Different Thickness. *International Vacuum Nanoelectronics Conference*; IEEE: Palo Alto, CA, USA, 2010; pp 153−154.
(66) Droubay, T.; Chambers, S. A. Surface-Sensitive Fe 2 p Photoemission Spectra for α- Fe 2 O 3 (0001) : The Influence of Symmetry and Crystal-Field Strength. *Phys. Rev. B: Condens. Matter Mater. Phys.* **2001**, *64* (20), 205414.
(67) Fishman, Z. S.; He, Y.; Yang, K. R.; Lounsbury, A. W.; Zhu, J.; Tran, T. M.; Zimmerman, J. B.; Batista, V. S.; Pfefferle, L. D. Hard Templating Ultrathin Polycrystalline Hematite Nanosheets: Effect of Nano-Dimension on CO $_2$ to CO Conversion via the Reverse Water-Gas Shift Reaction. *Nanoscale* **2017**, *9* (35), 12984−12995.
(68) Chang, C.-Y.; Wang, C.-H.; Tseng, C.-J.; Cheng, K.-W.; Hourng, L.-W.; Tsai, B.-T. Self-Oriented Iron Oxide Nanorod Array Thin Film for Photoelectrochemical Hydrogen Production. *Int. J. Hydrogen Energy* **2012**, *37* (18), 13616−13622.
(69) Kim, J. Y.; Jang, J.-W.; Youn, D. H.; Magesh, G.; Lee, J. S. A Stable and Efficient Hematite Photoanode in a Neutral Electrolyte for Solar Water Splitting: Towards Stability Engineering. *Adv. Energy Mater.* **2014**, *4* (13), 1400476.
(70) Manikandan, V.; Anushkkaran, P.; Hwang, I.-S.; Chae, W.-S.; Lee, H.-H.; Choi, S. H.; Mahadik, M. A.; Jang, J. S. Synergistic Role of In-Situ Zr-Doping and Cobalt Oxide Cocatalysts on Photocatalytic Bacterial Inactivation and Organic Pollutants Removal over Template-Free Fe2O3 Nanorods. *Chemosphere* **2023**, *310*, 136825.
(71) Lee, C.-Y.; Wang, L.; Kado, Y.; Killian, M. S.; Schmuki, P. Anodic Nanotubular/Porous Hematite Photoanode for Solar Water Splitting: Substantial Effect of Iron Substrate Purity. *ChemSusChem* **2014**, *7* (3), 934−940.
(72) Lucas-Granados, B.; Sánchez-Tovar, R.; Fernández-Domene, R. M.; García-Antón, J. Study of the Annealing Conditions and Photoelectrochemical Characterization of a New Iron Oxide Bi-Layered Nanostructure for Water Splitting. *Sol. Energy Mater. Sol. Cells* **2016**, *153*, 68−77.
(73) Jun, H.; Im, B.; Kim, J. Y.; Im, Y.-O.; Jang, J.-W.; Kim, E. S.; Kim, J. Y.; Kang, H. J.; Hong, S. J.; Lee, J. S. Photoelectrochemical Water Splitting over Ordered Honeycomb Hematite Electrodes Stabilized by Alumina Shielding. *Energy Environ. Sci.* **2012**, *5* (4), 6375−6382.
(74) Shen, S.; Jiang, J.; Guo, P.; Kronawitter, C. X.; Mao, S. S.; Guo, L. Effect of Cr Doping on the Photoelectrochemical Performance of Hematite Nanorod Photoanodes. *Nano Energy* **2012**, *1* (5), 732−741.
(75) Malviya, K. D.; Dotan, H.; Yoon, K. R.; Kim, I.-D.; Rothschild, A. Rigorous Substrate Cleaning Process for Reproducible Thin Film Hematite (α-Fe $_2$ O $_3$) Photoanodes. *J. Mater. Res.* **2016**, *31* (11), 1565−1573.
(76) Cai, J.; Xu, L.; Tang, X.; Kong, L.; Wang, J.; Wang, R.; Li, X.; Xie, Q.; Mao, K.; Pan, H. Role of lithium doping on α-Fe2O3 photoanode for enhanced photoelectrochemical water oxidation. *J. Alloys Compd.* **2022**, *915*, 165349.
(77) Zheng, J. Y.; Kang, M. J.; Song, G.; Son, S. I.; Suh, S. P.; Kim, C. W.; Kang, Y. S. Morphology evolution of dendritic Fe wire array by electrodeposition, and photoelectrochemical properties of α-Fe2O3 dendritic wire array. *CrystEngComm* **2012**, *14* (20), 6957.
(78) Ling, Y.; Wang, G.; Wheeler, D. A.; Zhang, J. Z.; Li, Y. Sn-Doped Hematite Nanostructures for Photoelectrochemical Water Splitting. *Nano Lett.* **2011**, *11* (5), 2119−2125.
(79) Rozana, M.; Abdul Razak, K.; Yew, C. K.; Lockman, Z.; Kawamura, G.; Matsuda, A. Annealing Temperature-Dependent Crystallinity and Photocurrent Response of Anodic Nanoporous Iron Oxide Film. *J. Mater. Res.* **2016**, *31* (12), 1681−1690.
(80) Vincent, T.; Gross, M.; Dotan, H.; Rothschild, A. Thermally Oxidized Iron Oxide Nanoarchitectures for Hydrogen Production by Solar-Induced Water Splitting. *Int. J. Hydrogen Energy* **2012**, *37* (9), 8102−8109.
(81) Chen, M.; Zhao, E.; Yan, Q.; Hu, Z.; Xiao, X.; Chen, D. The Effect of Crystal Face of Fe2O3 on the Electrochemical Performance for Lithium-Ion Batteries. *Sci. Rep.* **2016**, *6* (1), 29381.
(82) Liu, J.; Cai, Y. Y.; Tian, Z. F.; Ruan, G. S.; Ye, Y. X.; Liang, C. H.; Shao, G. S. Highly Oriented Ge-Doped Hematite Nanosheet Arrays for Photoelectrochemical Water Oxidation. *Nano Energy* **2014**, *9*, 282−290.
(83) Iandolo, B.; Wickman, B.; Zorić, I.; Hellman, A. The Rise of Hematite: Origin and Strategies to Reduce the High Onset Potential for the Oxygen Evolution Reaction. *J. Mater. Chem. A* **2015**, *3* (33), 16896−16912.
(84) Kay, A.; Cesar, I.; Grätzel, M. New Benchmark for Water Photooxidation by Nanostructured α-Fe $_2$ O $_3$ Films. *J. Am. Chem. Soc.* **2006**, *128* (49), 15714−15721.

https://doi.org/10.1021/acsomega.3c05726
ACS Omega 2023, 8, 38607−38618

(85) Sanchez, C.; Sieber, K. D.; Somorjai, G. A. The photoelectrochemistry of niobium doped α-Fe2O3. *J. Electroanal. Chem. Interfacial Electrochem.* **1988**, *252* (2), 269−290.
(86) Engel, J.; Tuller, H. L. The Electrical Conductivity of Thin Film Donor Doped Hematite: From Insulator to Semiconductor by Defect Modulation. *Phys. Chem. Chem. Phys.* **2014**, *16* (23), 11374.
(87) Bagheli, S.; Fadafan, H. K.; Orimi, R. L.; Ghaemi, M. Synthesis and Experimental Investigation of the Electrical Conductivity of Water Based Magnetite Nanofluids. *Powder Technol.* **2015**, *274*, 426−430.
(88) Miles, P. A.; Westphal, W. B.; Von Hippel, A. Dielectric Spectroscopy of Ferromagnetic Semiconductors. *Rev. Mod. Phys.* **1957**, *29* (3), 279−307.
(89) Tamirat, A. G.; Su, W.-N.; Dubale, A. A.; Chen, H.-M.; Hwang, B.-J. Photoelectrochemical Water Splitting at Low Applied Potential Using a NiOOH Coated Codoped (Sn, Zr) α-Fe $_2$ O $_3$ Photoanode. *J. Mater. Chem. A* **2015**, *3* (11), 5949−5961.
(90) Boudoire, F.; Toth, R.; Heier, J.; Braun, A.; Constable, E. C. Photonic Light Trapping in Self-Organized All-Oxide Microspheroids Impacts Photoelectrochemical Water Splitting. *Energy Environ. Sci.* **2014**, *7* (8), 2680−2688.
(91) Kennedy, J. H.; Frese, K. W. Flatband Potentials and Donor Densities of Polycrystalline α - Fe2 O 3 Determined from Mott-Schottky Plots. *J. Electrochem. Soc.* **1978**, *125* (5), 723−726.
(92) Wang, G.; Ling, Y.; Wheeler, D. A.; George, K. E. N.; Horsley, K.; Heske, C.; Zhang, J. Z.; Li, Y. Facile Synthesis of Highly Photoactive α-Fe $_2$ O $_3$ -Based Films for Water Oxidation. *Nano Lett.* **2011**, *11* (8), 3503−3509.
(93) Yan, D.; Tao, J.; Kisslinger, K.; Cen, J.; Wu, Q.; Orlov, A.; Liu, M. The Role of the Domain Size and Titanium Dopant in Nanocrystalline Hematite Thin Films for Water Photolysis. *Nanoscale* **2015**, *7* (44), 18515−18523.
(94) Dias, P.; Vilanova, A.; Lopes, T.; Andrade, L.; Mendes, A. Extremely Stable Bare Hematite Photoanode for Solar Water Splitting. *Nano Energy* **2016**, *23*, 70−79.
(95) Sivula, K.; Le Formal, F.; Grätzel, M. Solar Water Splitting: Progress Using Hematite (α-Fe2O3) Photoelectrodes. *ChemSusChem* **2011**, *4* (4), 432−449.
(96) Su, J.; Wang, J.; Liu, C.; Feng, B.; Chen, Y.; Guo, L. On the Role of Metal Atom Doping in Hematite for Improved Photoelectrochemical Properties: A Comparison Study. *RSC Adv.* **2016**, *6* (104), 101745−101751.
(97) Borse, P. H.; Jun, H.; Choi, S. H.; Hong, S. J.; Lee, J. S. Phase and Photoelectrochemical Behavior of Solution-Processed Fe2O3 Nanocrystals for Oxidation of Water under Solar Light. *Appl. Phys. Lett.* **2008**, *93* (17), 173103.
(98) Kim, J. Y.; Jun, H.; Hong, S. J.; Kim, H. G.; Lee, J. S. Charge Transfer in Iron Oxide Photoanode Modified with Carbon Nanotubes for Photoelectrochemical Water Oxidation: An Electrochemical Impedance Study. *Int. J. Hydrogen Energy* **2011**, *36* (16), 9462−9468.
(99) Shimizu, K.; Boily, J.-F. Electrochemical Signatures of Crystallographic Orientation and Counterion Binding at the Hematite/Water Interface. *J. Phys. Chem. C* **2015**, *119* (11), 5988−5994.
(100) Chatman, S.; Zarzycki, P.; Rosso, K. M. Surface potentials of (001), (012), (113) hematite (α-Fe2O3) crystal faces in aqueous solution. *Phys. Chem. Chem. Phys.* **2013**, *15* (33), 13911−13921.
(101) Venema, P.; Hiemstra, T.; Weidler, P. G.; van Riemsdijk, W. H. Intrinsic Proton Affinity of Reactive Surface Groups of Metal (Hydr)Oxides: Application to Iron (Hydr)Oxides. *J. Colloid Interface Sci.* **1998**, *198* (2), 282−295.
(102) Zhang, X.; Cao, C.; Bieberle-Hütter, A. Orientation Sensitivity of Oxygen Evolution Reaction on Hematite. *J. Phys. Chem. C* **2016**, *120* (50), 28694−28700.
(103) Shrimali, K.; Jin, J.; Hassas, B. V.; Wang, X.; Miller, J. D. The Surface State of Hematite and Its Wetting Characteristics. *J. Colloid Interface Sci.* **2016**, *477*, 16−24.

https://doi.org/10.1021/acsomega.3c05726
ACS Omega 2023, 8, 38607−38618